

Ultra-fast multi-qubit global-entangling gates without individual addressing of trapped ions

Kaizhao Wang,^{1,*} Jing-Fan Yu,^{2,*} Pengfei Wang,^{1,3} Chunyang Luan,¹ Jing-Ning Zhang,³ and Kihwan Kim^{1,3,4}

¹*State Key Laboratory of Low Dimensional Quantum Physics,
Department of Physics, Tsinghua University, Beijing 100084, China*

²*Institute for Interdisciplinary Information Sciences,
Tsinghua University, Beijing 100084, P. R. China*

³*Beijing Academy of Quantum Information Sciences, Beijing 100193, China*

⁴*Frontier Science Center for Quantum Information, Beijing 100084, People's Republic of China*

(Dated: January 19, 2022)

We propose and study how to increase the speed of the entangling gates with trapped ions while maintaining high fidelities from two aspects. First, we find a scheme to increase the speed of a two-qubit gate without the limitation of the trap frequency, which was considered the fundamental limit. Second, we simultaneously study the possibility and speed limit in applying entangling gates for more than two qubits, the global entangling gates. For the speedup, we explore modulating various control parameters such as phases and intensities, and applying multiple-frequency laser beams for the gate operations. In particular, in order to avoid infinite terms from carrier transitions, we focus on phase-insensitive gates, equivalent to light shift gates. We find that if phase modulation is included, the gate speed can be increased without the problem of infidelity caused by excessively large excitation of motional mode beyond the limit of Lamb-Dicke approximation. We also find that, by combining phase and intensity modulations, global entangling gates can be performed close to the limit of the trap frequency without individual addressing requirements. Furthermore, our gates are robust to the fluctuation of initial motional phases which are considered uncontrollable in the phase-insensitive gate scheme.

I. INTRODUCTION

Quantum computers can provide solutions for certain complex problems intractable by classical computers. A trapped-ion system is one of the most promising physical platforms to realize a practical quantum computer [1–4]. The longest coherence time of single-qubits [5, 6] and the highest fidelity of the entangling gates [7–9] among any other physical platforms have been demonstrated in trapped-ion systems. Due to the long coherence time of a trapped-ion qubit, the number of gates before decoherence can be in the order of 10^8 , which is in the leading position among potential physical platforms for quantum computers. However, the speeds of entangling gates in the trapped-ion system can be considered relatively slow, which would limit the application of some quantum algorithms for practical purposes. There have been many theoretical proposals and studies to speed up the trapped-ion entangling gates [10–15]. Recently, the experimental realizations of such fast quantum gates have been demonstrated with trapped ions [16–18]. Apart from speeding up the gate, by taking advantage of the full-connectivity of trapped ion system [19–21], simultaneous operations on more than two qubits [22–25] such as parallel gates and global gates have been intensively studied to shorten the running time of quantum algorithms.

The quantum entangling gates with trapped ion-qubits are primarily performed through the coupling of vibra-

tional modes, where the speed of the gates is mainly limited by the frequencies of the relevant vibrational modes. The duration of two-qubit gates has been pushed to $1.6 \mu s$, which is around 3 times the period of the axial center of mass mode, without serious loss in fidelity [16]. A faster gate of 480 ns, slightly less than one motional period, has also been demonstrated, but the fidelity is much lower owing to the high excitation of vibrational modes beyond the Lamb-Dicke regime [13, 16]. For the transverse modes, the duration of the two-qubit gates is significantly slowed down due to the relatively small spacing of vibrational modes [17]. Apart from that, the fast multiple-qubit parallel or global gates have not yet been thoroughly explored [22, 23].

In this work, we present solutions of the two-qubit gate with the duration of less than one motional period without the out-of-Lamb-Dicke-regime problem by taking advantage of phase-modulation rather than intensity-modulation applied in the previous work [13, 16]. We also find the scheme of realizing fast global gates on more than two qubits. We investigate the optimal conditions of the global fast gates with minimal control parameters without individual addressing, which is favorable for experimental realization. In principle, with individual control of laser parameters, high laser intensity and a large number of segments, we are able to realize global entangling gates faster than one motional period similar to the two-qubit gate. Without individual control, we numerically find the solutions of global entangling gates with the duration comparable to one vibrational period for three and four qubits, where we combine both phase and intensity modulations. Our solutions are consistent with

* These two authors contributed equally to the work

the theoretical bound estimated by the multi-frequency methods [24].

II. THEORY

A. Theoretical framework for entangling gates in a linear chain of ions

For trapped-ion quantum computation, qubit states are encoded in internal energy levels of the ions which are typically trapped in linear Paul traps. With properly controlled laser beams, we first entangle qubit states with collective vibrational modes and use these collective motions as information bus to entangle different qubits. At the end of the gate operation, we disentangle the qubit and motional modes. Two main types of entangling gates

used with trapped ions are $\hat{\sigma}_{\phi_S}\hat{\sigma}_{\phi_S}$ gate [26, 27] and $\hat{\sigma}_z\hat{\sigma}_z$ gate, where $\hat{\sigma}_{\phi_S} = \cos\phi_S\hat{\sigma}_x + \sin\phi_S\hat{\sigma}_y$, and $\hat{\sigma}_x, \hat{\sigma}_y$, and $\hat{\sigma}_z$ are the Pauli operators. With Raman laser beams for hyperfine qubits, $\hat{\sigma}_{\phi_S}\hat{\sigma}_{\phi_S}$ gates can be implemented in a phase-sensitive or phase-insensitive manner [28, 29]. We mainly focus on the phase-insensitive gate, which is formally equivalent [28, 29] to the $\hat{\sigma}_z\hat{\sigma}_z$ gate. In these gate schemes, we can take advantage of being able to derive the evolution in a mathematically clean way, in particular, the off-resonant carrier coupling terms [30].

To implement a phase-insensitive $\hat{\sigma}_{\phi_S}\hat{\sigma}_{\phi_S}$ gate, we shine two counter-propagating beams with equal but opposite detuning on the ions. Here we set $\phi_S = 0$, which leads to $\hat{\sigma}_x\hat{\sigma}_x$. In Fig. 1, we show the laser schemes for qubits encoded in sub-levels of the ground manifold, in which one Raman transition stimulated by two laser beams are effectively seen as one of the two counter-propagating beams. The Hamiltonian describing the phase-insensitive gate is written as

$$\hat{\mathcal{H}} = \sum_{j=1}^N \hbar\Omega \left[\cos(\mu t + \phi) - \sum_{m=0}^{N-1} \eta_{j,m} \sin(\mu t + \phi) (\hat{a}_m^\dagger e^{i\nu_m t} + \hat{a}_m e^{-i\nu_m t}) \right] \hat{\sigma}_x^j, \quad (1)$$

where j and m indicate the j^{th} ion and the m^{th} normal mode of the collective motion of the linear chain. We assume that ions have the same effective Rabi frequency Ω , phase ϕ , and detuning μ from the carrier frequency, $\mu = \nu_m + \delta_m$. \hat{a}_m and \hat{a}_m^\dagger are the annihilation and creation operators of the m^{th} motional mode, respectively, and ν_m are the corresponding frequencies of the vibrational modes with $\eta_{j,m} = b_{j,m}\eta_m$, where $b_{j,m}$ is the j^{th} entry of the eigen-vector of m^{th} normal mode and $\eta_m = \Delta k \sqrt{\frac{\hbar}{2M\nu_m}}$ is the Lamb-Dicke parameter of m^{th} mode. In the numerical calculation below, we set M to

be the mass of $^{171}\text{Yb}^+$ ion, and Δk is calculated assuming the direction of the two Raman beams are perpendicular and using the 355nm laser, thereby taking $\eta = 0.13$ after normalizing the center-of-mass mode frequency $\nu_0 = 2\pi$ MHz.

In the phase-insensitive gate, the carrier term, the first-term in Eq. (1), is commutative with the other terms, which leads to finite Magnus expansion in the time evolution. The evolution operator of the phase-insensitive gate is written as

$$\hat{U}(\tau) = \exp \left[-i\Phi \sum_{j=1}^N \hat{\sigma}_x^j + \sum_{j=1}^N \sum_{m=0}^{N-1} (\alpha_{j,m} \hat{a}_m^\dagger - \alpha_{j,m}^* \hat{a}_m) \hat{\sigma}_x^j - i \sum_{1 \leq i < j \leq N} \Theta_{ij} \hat{\sigma}_x^i \hat{\sigma}_x^j \right], \quad (2)$$

where the first term is a summation of single-qubit rotations with the uniform phase Φ for all the ions, the second is a summation of displacement operators in the motional phase space for all the ions j and normal motional modes m resulting in trajectories of $\alpha_{j,m}$ in the phase space, and the last term is the entangling term which corresponds to the geometric phases Θ_{ij} accumulated while moving in the phase space. The accumulated phase Θ_{ij} is proportional to the area enclosed in the trajectory. For our convenience, we further define the phase space displacement α_m and geometric phase Θ_m corresponding to the

m^{th} motional mode as

$$\alpha_{j,m} = b_{j,m} \alpha_m, \quad (3)$$

$$\Theta_{ij} = \sum_m b_{i,m} b_{j,m} \Theta_m. \quad (4)$$

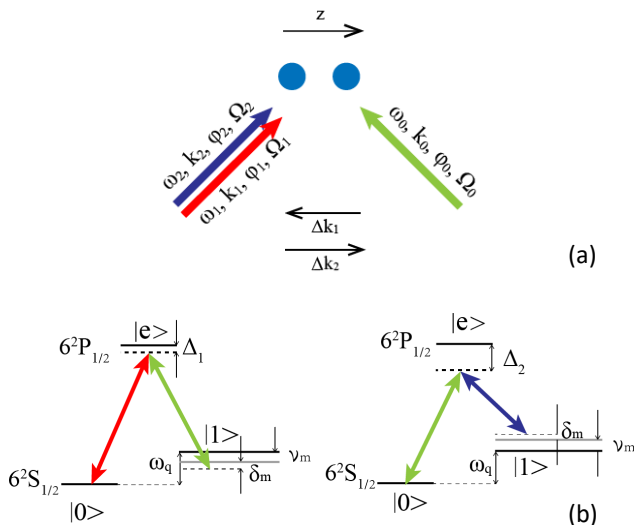


FIG. 1: Configuration for the phase-insensitive Mølmer-Sørensen gate. (a) One monochromatic and one bi-chromatic laser beams are applied on the target ions in the chain. Here ω_i , \mathbf{k}_i , ϕ_i , and Ω_i represent the angular frequency, wave-vector, phase, and Rabi-frequency of the three laser beams respectively, where $i = 0, 1, 2$. The effective wave-vectors of the two Raman transitions, $\Delta\mathbf{k}_1$ and $\Delta\mathbf{k}_2$, are in opposite directions. (b) The energy levels and couplings of the Raman laser beams for the gate process as an example of using $^{171}\text{Yb}^+$ ions, where $|0\rangle$, $|1\rangle$, and $|e\rangle$ represent the qubit levels and the intermediate level used in Raman transitions. Δ_1 and Δ_2 are the detuning from the intermediate level, and ω_q represents the qubit level splitting. ν_m is the motional frequency of the m^{th} mode, and δ_m is the detuning from it.

The explicit expression of α_m and Θ_m are written as

$$\alpha_m(\tau) = i\eta_m \int_0^\tau \Omega(t) \sin(\mu t + \phi(t)) e^{i\nu_m t} dt$$

$$\Theta_m(\tau) = -2\eta_m^2 \int_0^\tau \int_0^{t_1} \Omega(t_1)\Omega(t_2) \sin(\mu t_1 + \phi(t_1)) \sin(\mu t_2 + \phi(t_2)) \sin(\nu_m(t_1 - t_2)) dt_1 dt_2$$

For the case of two ions ($N = 2$), Eq. (1) and Eq. (2) describe the Hamiltonian and evolution operator of a standard two-qubit $\hat{\sigma}_x \hat{\sigma}_x$ gate. Typically, we set the laser detuning μ close to one of the motional mode frequency, for example, the center-of-mass mode frequency ν_0 , such that $|\delta_1| = |\mu - \nu_1| \ll |\mu - \nu_2| < |\mu + \nu_1| < |\mu + \nu_2|$, where ν_1 is the frequency of the stretch mode. Thus, we can neglect those terms rotating much faster than δ_0 according to the rotating-wave approximation (RWA). In order to disentangle the qubit and motional states, we have the gate time $\tau_g = \frac{2n\pi}{|\delta_1|}$, $n = 1, 2, 3, \dots$. The gate time is limited to dozens of times of the motional period to guarantee that the RWA is valid. For arbitrary number

of ions, we can entangle any pairs of ions with the phase of $\Theta_{ij} = \frac{\pi}{4}$, $\forall i, j$, which is referred as global entangling gate,

$$\hat{U}_{\text{global}} = \exp\left(-i\frac{\pi}{4} \sum_{i < j}^N \hat{\sigma}_x^i \hat{\sigma}_x^j\right), \quad (5)$$

when $|\delta_0| \ll |\mu - \nu_m|$ for all the other modes with $m > 0$. When the number of ions increases, the frequency spacing of vibrational modes reduces. It requires the value of δ_0 smaller, which leads longer duration for the gate. It has been shown that varying the laser parameters during the gate time provides possibilities to accelerate the gate, increase its robustness to some experiment parameters, and achieve more flexible entanglement for N -qubit simultaneously [24, 31–35].

B. Various Modulation Methods

Many modulating methods, such as phase modulation, intensity modulation, frequency modulation, and multi-frequency gate, have been discussed in various literature [24, 31, 33–35]. We can first abstractly treat the problem, regarding the laser waveform for the blue-sideband transition as an arbitrary complex function $f(t) = \Omega e^{-i(\mu t + \phi)}$ defined on $[0, \tau_g]$. and the waveform of the red-sideband transition would just be its complex conjugate. Here, the amplitude and the phase of this complex function are Ω , and $-(\mu t + \phi)$, respectively. Therefore, we can generate an arbitrary waveform with intensity modulation and phase modulation (or frequency modulation). Another way of decomposing a complex function defined on a finite real interval is using Fourier expansion as

$$f(t) = \sum_{n=-\infty}^{\infty} \Omega_n \exp(-in\omega t), \quad (6)$$

where $\Omega_n \in \mathbb{C}$ and $\omega = \frac{2\pi}{\tau_g}$. This Fourier expansion can be seen as applying multi-frequency components. From the completeness of Fourier series, we can also generate an arbitrary waveform with multi-frequency lasers.

The intensity and phase (or frequency) modulation and multi-frequency approach can provide the general control of laser beams. We can describe the operations with the controls in a matrix formalism and generally find an optimal solution by numerical searching. The Fourier expansion or equivalently the multi-frequency method can provide mathematically concise and simple formalism [24].

In the case of two-qubit gates and some circumstances of three-qubit gates, we can apply the multi-frequency method to analytically study their speed limitations. It is challenging to apply the analytical method for more complicated and general cases and we perform a numerical search to find solutions to fast gate with multiple ions. In the numerical searching, we notice that phase modulation is much more effective. Even in the ultra-fast regime,

where the duration of the gate is comparable to the period of the trap, with phase modulation, the trajectory in the phase space is more controllable, thereby being efficient to accumulate the desired geometric phase and also avoiding the out-of-Lamb-Dicke-regime problem occurred in the mere intensity modulation solutions [13, 16].

We can intuitively understand the advantage of phase modulation over intensity modulation as follows. The trajectory in the phase space $\alpha(\tau)$ for a vibrational mode can be expressed as

$$\alpha(\tau) \propto \int_0^\tau \Omega(t) \sin(\mu t + \phi(t)) e^{i\nu t} dt, \quad (7)$$

where ν is the frequency of the vibrational mode. For a certain segment starting at t_0 and lasting for τ , the displacement during this segment, $\Delta\alpha(t_0, \tau)$ is written as

$$\Delta\alpha(t_0, \tau) \propto \int_{t_0}^{t_0+\tau} \Omega \sin(\mu t + \phi) e^{i\nu t} dt. \quad (8)$$

For fixed t_0 and τ , the ending points of these displacements for different ϕ form an ellipse, and it can be easily proved that the shape of this ellipse is not dependent on t_0 . For most of the duration time τ , the ellipse's shape is relatively close to a circle, which means we can arbitrarily choose the direction to move as shown in Fig. 2 (a). However, merely changing the intensity will not change the direction of the displacement for fixed t_0 and τ as shown in Fig. 2 (b). With mere intensity modulation, the flexibility of changing direction is based on changing the duration of the segment τ . Thus, as shown in Fig. 2 (b), turning the trajectory is quite time-consuming. Therefore, it is intuitive that phase modulation enables us to control a desired efficient trajectory more flexibly, especially in the fast gate regime.

C. Numerical search for optimal gate schemes with intensity and phase modulation

We apply intensity and phase modulation to find optimal gate schemes for ultra-fast gates on multiple qubits. We consider a simple implementation without any individual control of ions. We also assume that the time-dependence of $\Omega(t)$ and $\phi(t)$ are implemented by piecewise functions. We can transfer this problem into an optimization problem by giving the infidelity of the gates. We characterize these gates by applying them to form Greenberger–Horne–Zeilinger states (GHZ states), and the fidelity of GHZ states can be a comprehensive characterization of the gate [23], where the infidelity ε can be written as

$$\begin{aligned} \varepsilon \approx & \frac{1}{4} \sum_{m=0}^{N-1} \sum_{j=1}^N |\alpha_{j,m}(\tau_g)|^2 \\ & + \sum_{i<j}^N \left(\Theta_{ij} - \frac{\pi}{4} \right)^2 + 3\Phi^2. \end{aligned} \quad (9)$$

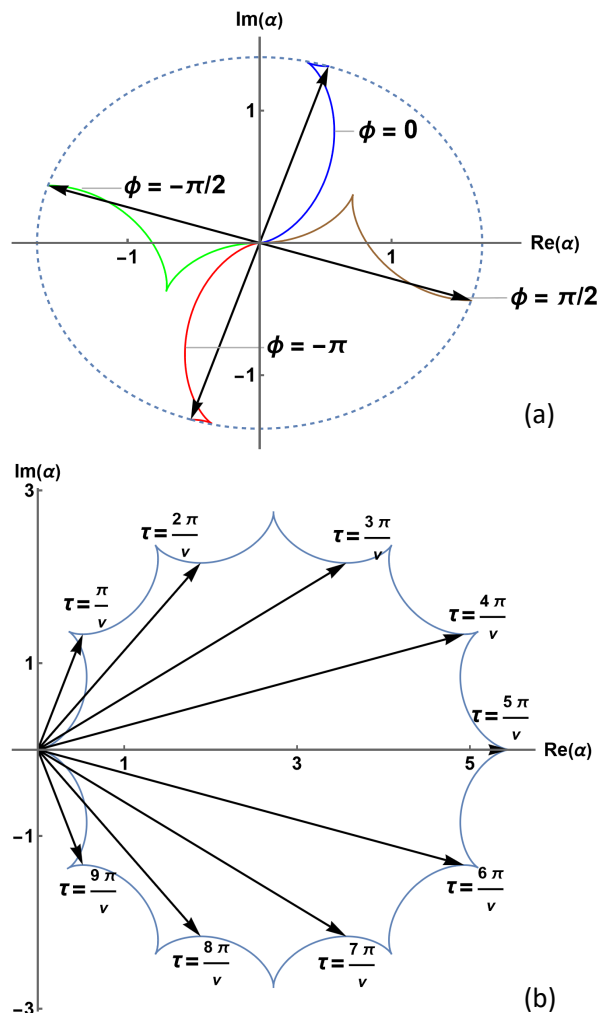


FIG. 2: The comparison between phase modulation and intensity modulation. (a) The control of the displacement direction by phase modulation. The ending points of displacements $\Delta\alpha$ (starting from the origin) forms an ellipse when the phase ϕ is changed from $-\pi$ to π . Therefore, modulating the phase can set the displacement to any direction. The figure is calculated for the conditions of $\mu = 1.2\nu$ and $\tau = \pi/\nu$. (b) The control of the displacement direction by intensity modulation in the phase space. With the intensity modulation, the direction of the displacement is only changed with time. Therefore, it is necessary to wait to change the direction, unlike the phase modulation can change the angle instantaneously. Moreover, the change of the displacement direction is restricted by roughly $[-0.41\pi, 0.41\pi]$ in any duration. The figure is calculated for the conditions of $\mu = 1.2\nu$.

Here the first two terms ensure that the phase space trajectories close at the end of the gate time with proper geometric phases accumulated, while the last one cor-

responds to the carrier constraint. Assuming that the piece-wise functions have N_{seg} segments, we can write the infidelity ε as a function of $3N_{\text{seg}} + 1$ parameters, μ , τ_k , Ω_k , ϕ_k , where μ is the laser's detuning, τ_k , Ω_k , and ϕ_k are the duration, effective Rabi frequency, and motional phase for the k^{th} segment respectively. By numerically optimizing the infidelity, we retain all the solutions with infidelity less than 1% as potential candidates of our gate. The initial parameter for the optimization is chosen randomly in an empirically sensible region. The dependency of the error function ε on the initial phase is periodic, and it is sufficient to make the gate robust to initial phase by setting $\varepsilon(\phi = 0) = \varepsilon(\phi = \frac{\pi}{4}) = \varepsilon(\phi = \frac{\pi}{2}) = 0$ (can be seen from Appendix B). Therefore, when including the initial phase robustness condition, we replace our error function with an average of the above three errors corresponding to the three different initial phases. We note that this numerical method allows us to compare the circumstances with merely phase modulation or intensity modulation taking into account experimental factors. We observe the phase modulation is more efficient than the intensity modulation as we discussed in section II B.

D. Fourier expansion formalism

As shown in Section II B, we can generate an arbitrary waveform with the Fourier expansion form, which provides an analytical way of understanding the speed limit of the ultra-fast gate on multiple ions for simple cases. For more general cases, however, the method also requires to use numerical search. We note that the method was mainly developed by the Ref. [24, 32].

We assume that the gate duration is τ_g . As the waveform is a function defined in $[0, \tau_g]$, we can Fourier expand it as

$$f_{\text{bsb}}(t) = \sum_{n=-\infty}^{\infty} \Omega_n \exp(-in\omega t), f_{\text{rsb}}(t) = f_{\text{bsb}}^*(t), \quad (10)$$

where we set $\omega = 2\pi/\tau_g$. Defining $\Omega_n = \Omega_n^r + i\Omega_n^i$, we can rewrite our effective Hamiltonian as

$$\hat{\mathcal{H}}_{\text{eff}} = \hat{\mathcal{H}}_{\text{car}} + \hat{\mathcal{H}}_{\text{mot}}, \quad (11)$$

where

$$\hat{\mathcal{H}}_{\text{car}} = \sum_{j=1}^N \hbar \hat{\sigma}_x^j \sum_{n=0}^{\infty} [\Omega_n^{rc} \cos(n\omega t) + \Omega_n^{ic} \sin(n\omega t)] \quad (12)$$

$$\hat{\mathcal{H}}_{\text{mot}} = \sum_{m=0}^{N-1} \sum_{j=1}^N \hbar \eta_{j,m} (\hat{a}_m^\dagger e^{i\nu_m t} + \hat{a}_m e^{-i\nu_m t}) \hat{\sigma}_x^j \sum_{n=0}^{\infty} [\Omega_n^{rm} \sin(n\omega t) + \Omega_n^{im} \cos(n\omega t)]. \quad (13)$$

where for $n \neq 0$,

$$\begin{aligned} \Omega_n^{rc} &= \Omega_n^r + \Omega_{-n}^r \\ \Omega_n^{ic} &= \Omega_n^i - \Omega_{-n}^i \\ \Omega_n^{rm} &= -\Omega_n^r + \Omega_{-n}^r \\ \Omega_n^{im} &= \Omega_n^i + \Omega_{-n}^i, \end{aligned}$$

and $\Omega_0^{rc} = \Omega_0^r$, $\Omega_0^{im} = \Omega_0^i$, $\Omega_0^{ic} = \Omega_0^{rm} = 0$.

We combine the terms corresponding to frequency $n\omega$ and $-n\omega$ in the above way. It can be seen that by including the negative frequency terms, the coefficients for the carrier and motional terms of the Hamiltonian are independent. The above evolution operator can therefore be written in matrix forms. As we could not deal with infinite terms, we will do a finite truncation from n_s to n_e . We define the vectors of $\vec{\Omega}^c$, $\vec{\Omega}^m$, \vec{T} , and \vec{a}_m with the dimension of $2(n_e - n_s + 1)$ and matrices θ_m with the dimension of $2(n_e - n_s + 1) \times 2(n_e - n_s + 1)$ as

$$\vec{\Omega}^{c(m)} = \begin{bmatrix} \vec{\Omega}^{ic(rm)} \\ \vec{\Omega}^{rc(im)} \end{bmatrix}; \vec{T} = \begin{bmatrix} \vec{T}^r \\ \vec{T}^i \end{bmatrix}; \quad (14)$$

$$\vec{a}_m = \begin{bmatrix} \vec{a}_m^r \\ \vec{a}_m^i \end{bmatrix}; \theta_m = \begin{bmatrix} \theta^{rr} & \theta^{ri} \\ \theta^{ir} & \theta^{ii} \end{bmatrix}, m = 0, 1, \dots, N-1 \quad (15)$$

where the explicit expression of each entry is given in Appendix A. To symmetrize θ_m , we define $\tilde{\theta}_m = (\theta_m + \theta_m^T)/2$. We can rewrite Φ , α_m , and Θ_m as

$$\Phi = \vec{T}^T \vec{\Omega}^c, \quad (16)$$

$$\alpha_m = \vec{a}_m^T \vec{\Omega}^m, \quad (17)$$

$$\Theta_m = \vec{\Omega}^{mT} \tilde{\theta}_m \vec{\Omega}^m. \quad (18)$$

For an ideal gate, we need to satisfy the constraints that both Φ and α_m are zero. It is noticeable that the matrix elements of \vec{T} are all zero except $T_0^r = \tau_g$ because of $\omega = 2\pi/\tau_g$ (see Appendix A). Therefore, the constraint, $\Phi = 0$, is fulfilled automatically. We also demand $\alpha_m = 0$ to disentangle the qubit states and motional states. We can rewrite the constraint more explicitly with real and imaginary parts of α_m as

$$L\vec{\Omega}^m = \vec{0}, \quad (19)$$

where L with dimension $2N \times 2(n_e - n_s + 1)$ is defined as

$$L_{m,j} = \begin{cases} \text{Re}\{(\vec{a}_m)_j\} & 0 \leq m \leq N-1 \\ \text{Im}\{(\vec{a}_{m-N})_j\} & N \leq m \leq 2N-1 \end{cases} \quad (20)$$

Solving the linear equations above, we can obtain a set of solutions as $\vec{\Omega}_1, \vec{\Omega}_2, \dots, \vec{\Omega}_l$. Define $K_{2(n_e - n_s + 1) \times l} = (\vec{\Omega}_1, \vec{\Omega}_2, \dots, \vec{\Omega}_l)$ which is a basis for the kernel of L , $\text{Ker}(L)$, and let $\dim(\text{Ker}(L)) = l$. Any vector in $\text{Ker}(L)$ can be represented as a linear combination of the basis vectors in K .

$$\vec{\Omega} = K\vec{x}, \quad \forall \vec{\Omega} \in \text{Ker}(L), \quad (21)$$

where \vec{x} is a l -dimensional real vector. Now, we can rewrite Eq. (18) as

$$\Theta_m = \vec{x}^T K^T \tilde{\theta}_m K \vec{x} = \vec{x}^T A_m \vec{x}, \quad (22)$$

where $A_m = K^T \tilde{\theta}_m K$. Therefore, by solving Eq. (19), we can obtain K thereby calculating A_m . Now, we need to find a l -dimensional real vector \vec{x} such that the quadratic form $\vec{x}^T A_m \vec{x}$ equals to our desired entangling phase.

In phase insensitive gate, the phase related to the qubit ϕ_s is insensitive to the optical path fluctuation, while the motional phase, ϕ can vary between different shots of experiments. Therefore, it is important to consider the gate's robustness against this initial phase fluctuation. To make the gate robust to its initial phase, we require both Ω^c and Ω^m to fulfill the requirement in Eq.(16)-Eq. (18) with an additional quadratic constraint,

$$\vec{\Omega}^{cT} \tilde{\theta}_m \vec{\Omega}^m = 0. \quad (23)$$

Detailed derivation of this part can be seen in Appendix B.

Applying the formalism described above, we can analyze some properties in the cases of 2-qubit and 3-qubit gate, which will be discussed in detail in section III. If we want to achieve an N -qubit gate with global beam, there would be $N - 1$ quadratic constraints to be solved, which requires numerical methods for $N \geq 3$. Even for the 3-qubit gate, to include the initial phase robustness condition, we also need to apply numerical search.

We can define our function to be optimized depending on different experiment constraints or desirable features. For instance, we can minimize the maximum value of the Rabi frequency during the gate time to make demanded laser power more achievable, or we can minimize the total pulse area, $\int_0^{\tau_g} \Omega(t) dt$, which is proportional to the scattering error induced by coupling to other levels.

The Fourier method can be both understood as applying multi-frequency lasers and continuous modulation of intensity and phase. Typically these modulations are realized in discrete steps of time. If we choose the intensities and phases at fixed time intervals, there will be significant errors caused by the discrete sampling. Here, we develop a sampling method such that the low-frequency Fourier components of the continuous and discrete one are equal. We also estimate the errors caused by the high-frequency components in the Fourier transform of the discrete waveform, which is orders of magnitude smaller (see details in Appendix C).

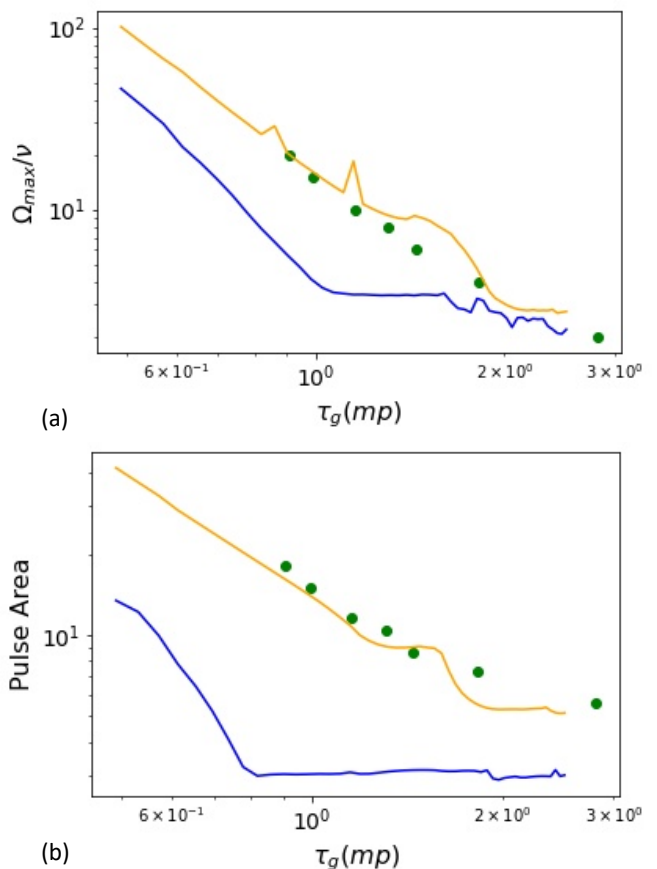


FIG. 3: The required maximum of Rabi frequency (Ω_{\max}) and pulse area ($\int_0^{\tau_g} \Omega(t) dt$) for ultra-fast two-qubit gate. (a) The relation between the duration of the gate and the maximum Rabi frequency. (b) The relation between the duration and pulse area. For both (a) and (b), green filled circles represent the results of numerical search for fixed Rabi frequencies with only phase modulation, while the other two curves are the results of numerical search based on the Fourier formalism under different constraints. For the orange line, the initial phase robustness condition is considered, while in the blue line, it is neglected.

III. RESULTS

A. Two-qubit gate

We have applied the numerical method discussed in II C to investigate the optimal pulse shapes with phase modulation for the ultra-fast two-qubit gate. We use the axial modes as a quantum bus to entangle qubits through all the calculations. The larger spacing of axial modes than that of the transverse modes is suitable for accelerating the gate. In numerical search using phase modulation, we bound the detuning μ between the center-of-mass mode and the stretch mode and include the constraints of no carrier coupling and robustness to initial

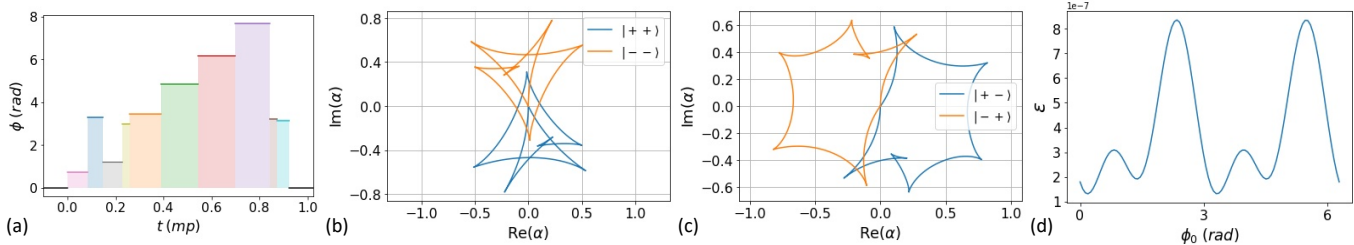


FIG. 4: Example of ultra-fast two-qubit gate corresponding to the leftmost green dots in Fig. 3. The entanglement is realized by applying the gate for the duration of $\tau_g \approx 0.93 \frac{2\pi}{\nu}$. The gate is performed at the detuning of $\mu \approx 1.49\nu$. (a) The modulated phases changing over time, which consist of ten-segments. (b) The trajectory in the phase space for the center-of-mass mode. (c) The trajectory in the phase space for the stretch mode. (d) The infidelity of the gate depending on the initial optical phase ϕ_0 , which is below 10^{-6} .

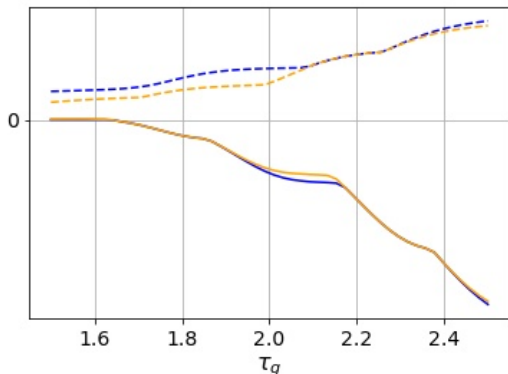


FIG. 5: The maximum and minimum eigenvalues of matrix from the Eq. (22) for Eq. (24). The dashed lines represent the maximum eigenvalues while the solid lines correspond to the minimum. The orange and blue colors represent with and without initial phase robustness circumstance respectively. As illustrated in the paper, the points where one of the lines cross zero indicate boundaries of speed limit for the three-qubit gate, which is 1.63 for both cases.

phases. The results are shown in the green dots of Fig. 3.

An example of ultra-fast two-qubit gate below one motional period, $\tau_g = 0.93 \frac{2\pi}{\nu}$, is shown in Fig. 4. In Fig. 4(a), we show the segmented phases of the gate. As can be seen from the trajectories in the phase space for both center of mass and stretch modes, shown in Fig. 4(b) and (c), respectively, the displacements are both less than 1, which clearly indicates that Lamb-Dicke approximation is valid. The infidelity of the gate is below 10^{-6} for any initial phase, which strongly indicates that the phase modulation has an advantage of accelerating the gate speed within the Lamb-Dicke regime.

We also investigate the scaling behavior of maximum Rabi-frequency and pulse area depending on the gate time with the method discussed in IID. For the 2-qubit gate, the waveform with the lowest Rabi-frequency can be calculated analytically applying the formalism described

above as discussed in Ref. [24]. The entangling phase $\Theta_{12} = \frac{1}{2}(\Theta_{m=0} - \Theta_{m=1})$ for a standard $\hat{\sigma}_x \hat{\sigma}_x$ gate of two qubits is $\frac{\pi}{4}$. We solve the quadratic equation (22) related to $\Theta_{12} = \pi/4$ and find the largest eigenvalue and the corresponding eigenvector of its coefficient matrix, $A_0 - A_1$, which leads to the solution with the lowest Rabi-frequency.

We note that the result provides the smallest norm of the Rabi frequencies of multiple frequency components. As mentioned in IID, the multi-frequency method can be understood as the Rabi-frequency and phase modulation. In that case, the maximum Rabi-frequency in the gate sequence or the pulse area, related to the actual laser intensity and scattering errors, respectively, can be meaningful. Thus, we apply the numerical method of IID with the cost function as maximum Rabi frequency Ω_{\max} or pulse area. The results are shown in Fig. 3(a) and (b) depending on the gate time for Ω_{\max} and pulse area, respectively. The orange (blue) curves correspond to the cases of (not) considering the initial phase robustness condition. It is important to include the initial phase robustness for the experiment with the phase insensitive gates. As the fidelity can be halved, if the initial phase is drifted by $\pi/2$ (as can be seen in Appendix B).

We can see that the dependence of maximum Rabi-frequency and pulse area on the gate time is consistent for both phase modulation and Fourier methods. In principle, the gate time is only limited by the maximum available Rabi-frequency for the two-qubit gate. Furthermore, if the optical phase can be stabilized, the required maximum Rabi-frequency can be further reduced as shown in the blue curves of Fig. 3.

B. Three-qubit gate

We study the lower limit of the gate time for the three-qubit global-entangling gates by using the Fourier method discussed in section IID. For three-qubit gate, even without the initial phase robustness, it is not possible to analytically find the most efficient waveform, but we can calculate the existence of a solution of Eq. (22) de-

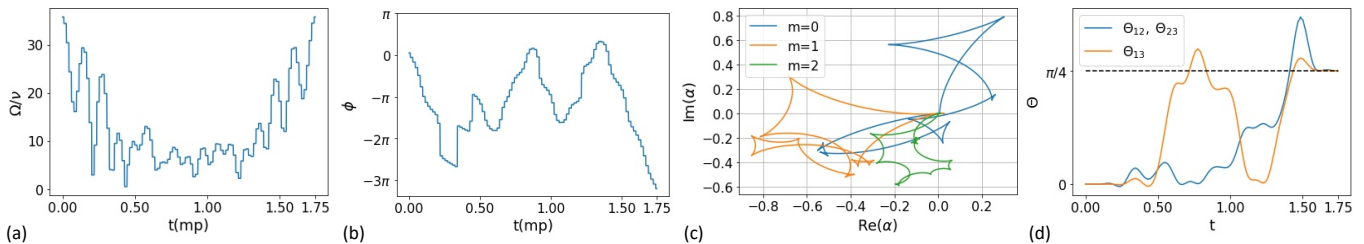


FIG. 6: Example of ultra-fast three-qubit global-entangling gate with initial phase robustness. The GHZ state of three qubits is produced by applying the gate for the duration of $\tau_g \approx 1.75 \frac{2\pi}{\nu}$. The gate is performed at the detuning of $\mu \approx 0.93\nu$. (a) The modulated Rabi frequencies and (b) phases changing over time with the 100 steps (c) The trajectories of the leftmost ion for three motional modes in the phase space. The center-of-mass ($m = 0$) mode, stretch mode ($m = 1$), and zigzag mode ($m = 2$) are represented by blue, orange and green colors, respectively. (d) The evolution of the accumulated geometric phase.

pending on the gate time, which provides the lower bound of the gate time. The phase requirement for the global-entangling gate of three-qubit system, $\Theta_{12} = \Theta_{13} = \Theta_{23} = \frac{\pi}{4}$, can be written as

$$\Theta_{m=1} - \Theta_{m=2} = 0 \quad (24)$$

$$\Theta_{m=0} - \Theta_{m=1} = \frac{3\pi}{4} \quad (25)$$

The quadratic equation (22) for the Eq. (24) can be addressed by dividing the eigen-vectors of the matrix $A_1 - A_2$ into two groups, one with positive eigenvalues the other with negative ones. As long as there are both positive and negative eigenvalues we can always find the solution of \vec{x} [24]. Therefore, we can find the lower bound of the gate time by solving the eigenvalue equation of the matrix $A_1 - A_2$ depending on different τ_g and seeking for the transition point when the corresponding matrix becomes semi-positive or semi-negative definite. The maximum and minimum eigenvalues of the matrix are shown as the blue dashed and solid lines of Fig. 5, respectively, where the corresponding matrix becomes positive-definite at around 1.63 times of the motional period.

While taking the initial phase robustness condition into account, as explained in IID, we need to include an additional quadratic condition, Eq. (23), apart from fulfilling Eqs. (16-18) for both $\tilde{\Omega}^c$ and $\tilde{\Omega}^m$, which are Eqs. (B3-B6). Because of the additional quadratic constraint, we can no longer find the boundary by looking at the zeros of eigenvalues. However, we can first neglect the additional quadratic constraint, Eq. (23), and find a lower boundary for the three-qubit gate robust to initial phase, which might not be the tight boundary. The corresponding matrix becomes positive-definite at around 1.63 times of the motional period shown in the orange curve of Fig. 5. We explore the tight boundary by numerically finding solutions, which occur at approximately 1.7 times of the motional period. Together with the 1.63 times of motional period lower boundary, the actual limit is indicated to be slightly below 1.7 times of the motional period.

We can realize the three-qubit global gates up to the

global phase by setting the geometric phases as $\Theta_{12} = \Theta_{23} = \frac{\pi}{4}$ and $\Theta_{13} = -\frac{3\pi}{4}$. It could be more efficient because it does not need to equalize phases between the intrinsic symmetric phases of $\Theta_{12} = \Theta_{23}$ and Θ_{13} . However, in the eigenvalue methods, we do not observe an improved lower limit.

An example of a fast three-qubit global-gate with duration $\tau_g = 1.75 \frac{2\pi}{\nu}$, is shown in Fig. 6. In Fig. 6(a) and (b), we show the segmented Rabi-frequencies and phases of the gate. As can be seen from the trajectories of the leftmost ion in the phase space for all the three motional modes, shown in Fig. 6 (c), the requirement of Lamb-Dicke approximation is held. The evolution of the entangling phases is shown in Fig. 6 (d), which all end at $\frac{\pi}{4}$ as expected. Here, we note that the Rabi-frequencies and phases of the gate in a hundred segments are carefully chosen by the method described in Appendix C. Applying the method, we obtain the gate of segmented sequence equivalent to continuous intensity and phase modulation.

C. Four-qubit Gates

The duration for the four-qubit global gate cannot be shorter than that of three-qubit gate because the constraints in four-qubit gate contain those of three-qubit gate. However, it is hard to calculate a tighter bound by solving eigenvalue equations, Eq. (22), because there are more than two quadratic constraints in four-qubit case. Thus, we numerically search the solution using the package of python, Sequential Least Squares Programming [36], minimizing Ω_{max} . For the case without initial phase robustness circumstance Eqs. (16-18) are set to be the constraints. From the blue curve of Fig. 7, we find solutions whose gate time is 1.705 times of the motional period, and infidelity is less than 10^{-13} without initial phase robustness. Therefore there should be a lower bound between 1.63 (three-qubit bound) and 1.705 of the motional period.

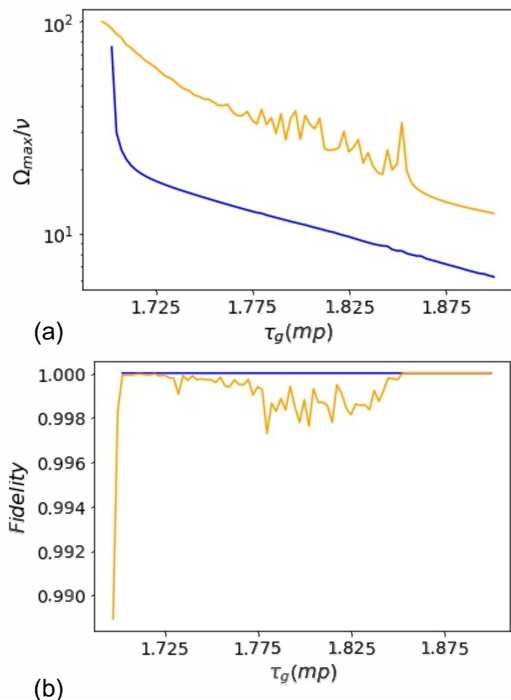


FIG. 7: Required maximum Rabi-frequencies and fidelities for fast global entangling gates with four qubits. The orange and the blue lines represent the cases with and without including the robustness of initial phases, respectively. The lower bound without initial phase robustness is around 1.7. The lower bound with initial phase robustness can be around 1.85 based on the convergence of numerical search. We note that there exist the solutions of the gates with around 10^{-4} levels of infidelity below 1.85, but there is no such solutions below 1.7. The fidelity is calculate by Eq. (9).

For the case with initial phase robustness circumstance Eqs. (B3-B6) are set to be the constraints. We find a solution with initial phase robustness circumstance whose gate time is 1.8575 of the motional period and infidelity is smaller than 10^{-11} . In the case of 1.705-1.8575 motional period, we can find solution whose infidelity is around 10^{-4} , but it is hard to find solution with better fidelity. in the case of less than 1.705 motional period, the fidelity of the gates we found decays rapidly, which corresponds with the case without initial phase robustness circumstance.

An example of a fast four-qubit global-gate with dura-

tion $\tau_g = 1.875 \frac{2\pi}{\nu}$, is shown in Fig. 8. In Fig. 8(a) and (b), we show the segmented Rabi-frequencies and phases of the gate. As can be seen from the trajectories of the leftmost ion in the phase space for all the four motional modes, shown in Fig. 8 (c), the requirement of Lamb-Dicke approximation is also held. The evolution of the entangling phases is shown in Fig. 8 (d), which all end at $\frac{\pi}{4}$ as expected. Here, we note that the Rabi-frequencies and phases of the gate in a hundred segments are carefully chosen by the method described in Appendix C.

IV. CONCLUSION AND OUTLOOK

We have presented the schemes of realizing ultra-fast global-entangling gate without individual addressing. By applying mainly phase modulation, we have found two-qubit gates below one motional period without exciting the vibrational modes out of the Lamb-Dicke regime, which is considered as the main fundamental error for gate at such speed level. By utilizing both intensity and phase modulation, which is equivalent to the multi-frequency methods [24], similar results can be achieved. The multi-frequency methods are applied to three- and four-qubit systems, where we have found the speed limit of the global gates. We present the examples of the global-gates near the speed limit for three- and four-qubit systems. Our numerical methods can be applied to a larger number of qubits and reveal the speed limitation of the global gates without individual addressing.

We believe that, with the capability of controlling individual qubits, the speed of the gate can be further improved, but it may require more computational power to optimize larger number of control variables [23]. We mainly include the robustness condition for the initial phase fluctuation, which is essential for the phase-insensitive gates. It could be interesting to explore the speed limit of the phase-sensitive gates, where instead of initial phase fluctuation, the carrier coupling could introduce a serious limitation [24].

ACKNOWLEDGMENTS

KZW and JFY are equally contributed to the work. This work was supported by the National Key Research and Development Program of China under Grants No. 2016YFA0301900 and No. 2016YFA0301901, the National Natural Science Foundation of China Grants No. 92065205, and No. 11974200.

-
- [1] T. D. Ladd, F. Jelezko, R. Laflamme, Y. Nakamura, C. Monroe, and J. L. O'Brien, *Quantum computers*, *Nature* **464**, 45 (2010).
 [2] C. Monroe and J. Kim, *Scaling the ion trap quantum*

- processor*, *Science* **339**, 1164 (2013).
 [3] H. Häffner, C. F. Roos, and R. Blatt, *Quantum computing with trapped ions*, *Phys. Rep.* (2008).
 [4] R. Blatt and C. F. Roos, *Quantum simulations with*

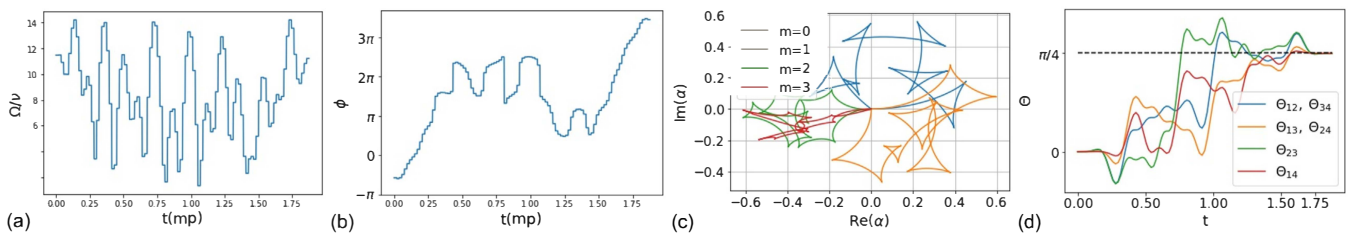


FIG. 8: Example of ultra-fast four-qubit global-entangling gate with initial phase robustness. The GHZ state of four qubits is produced by applying the gate for the duration of $\tau_g = 1.875 \frac{2\pi}{\nu}$. The gate is performed at the detuning of $\mu = 5\nu$. (a) The modulated Rabi frequencies and (b) phases changing over time with the hundred steps. (c) The trajectories of the four motional modes of the left most ion in the phase space. (d) The evolution of the accumulated geometric phase.

- trapped ions, *Nat. Phys.* (2012).
- [5] Y. Wang, M. Um, J. Zhang, S. An, M. Lyu, J.-N. Zhang, L.-M. Duan, D. Yum, and K. Kim, Single-qubit quantum memory exceeding ten-minute coherence time, *Nature Photonics* **11**, 646 (2017).
- [6] P. Wang, C.-Y. Luan, M. Qiao, M. Um, J. Zhang, Y. Wang, X. Yuan, M. Gu, J. Zhang, and K. Kim, Single ion qubit with estimated coherence time exceeding one hour, *Nat. Commun.* **12**, 233 (2021).
- [7] C. J. Ballance, T. P. Harty, N. M. Linke, M. A. Sepiol, and D. M. Lucas, High-fidelity quantum logic gates using trapped-ion hyperfine qubits, *Phys. Rev. Lett.* **117**, 060504 (2016).
- [8] J. P. Gaebler, T. R. Tan, Y. Lin, Y. Wan, R. Bowler, A. C. Keith, S. Glancy, K. Coakley, E. Knill, D. Leibfried, and D. J. Wineland, High-fidelity universal gate set for $9\text{be}+$ ion qubits, *Phys. Rev. Lett.* **117**, 060505 (2016).
- [9] C. R. Clark, H. N. Tinkey, B. C. Sawyer, A. M. Meier, K. A. Burkhardt, C. M. Seck, C. M. Shappert, N. D. Guise, C. E. Volin, S. D. Fallek, H. T. Hayden, W. G. Rellergert, and K. R. Brown, High-Fidelity Bell-State preparation with $^{40}\text{Ca}^+$ optical qubits, *Phys. Rev. Lett.* **127**, 130505 (2021).
- [10] J. J. García-Ripoll, P. Zoller, and J. I. Cirac, Coherent control of trapped ions using off-resonant lasers, *Phys. Rev. A* **71**, 062309 (2005).
- [11] J. J. García-Ripoll, P. Zoller, and J. I. Cirac, Speed optimized two-qubit gates with laser coherent control techniques for ion trap quantum computing, *Phys. Rev. Lett.* **91**, 157901 (2003).
- [12] L.-M. Duan, Scaling ion trap quantum computation through fast quantum gates, *Phys. Rev. Lett.* **93**, 100502 (2004).
- [13] A. M. Steane, G. Imreh, J. P. Home, and D. Leibfried, Pulsed force sequences for fast phase-insensitive quantum gates in trapped ions, *New J. Phys.* **16**, 053049 (2014).
- [14] E. Torrontegui, D. Heinrich, M. I. Hussain, R. Blatt, and J. J. García-Ripoll, Ultra-fast two-qubit ion gate using sequences of resonant pulses, *New J. Phys.* **22**, 103024 (2020).
- [15] Z. Mehdi, A. K. Ratcliffe, and J. J. Hope, Fast entangling gates in long ion chains, *Phys. Rev. Res.* **3** (2021).
- [16] V. M. Schafer, C. J. Ballance, K. Thirumalai, L. J. Stephenson, T. G. Ballance, A. M. Steane, and D. M. Lucas, Fast quantum logic gates with trapped-ion qubits, *Nature* **555**, 75 (2018).
- [17] J. D. Wong-Campos, S. A. Moses, K. G. Johnson, and C. Monroe, Demonstration of two-atom entanglement with ultrafast optical pulses, *Phys. Rev. Lett.* **119**, 230501 (2017).
- [18] C. Zhang, F. Pokorny, W. Li, G. Higgins, A. Pöschl, I. Lesanovsky, and M. Hennrich, Submicrosecond entangling gate between trapped ions via rydberg interaction, *Nature* **580**, 345 (2020).
- [19] T. Choi, S. Debnath, T. A. Manning, C. Figgatt, Z.-X. Gong, L.-M. Duan, and C. Monroe, Optimal quantum control of multimode couplings between trapped ion qubits for scalable entanglement, *Phys. Rev. Lett.* **112**, 190502 (2014).
- [20] S. Debnath, N. M. Linke, C. Figgatt, K. A. Landsman, K. Wright, and C. Monroe, Demonstration of a small programmable quantum computer with atomic qubits, *Nature* **536**, 63 (2016).
- [21] N. M. Linke, D. Maslov, M. Roetteler, S. Debnath, C. Figgatt, K. A. Landsman, K. Wright, and C. Monroe, Experimental comparison of two quantum computing architectures, *Proc. Natl. Acad. Sci. U. S. A.* **114**, 3305 (2017).
- [22] C. Figgatt, A. Ostrander, N. M. Linke, K. A. Landsman, D. Zhu, D. Maslov, and C. Monroe, Parallel entangling operations on a universal ion-trap quantum computer, *Nature* **572**, 368 (2019).
- [23] Y. Lu, S. Zhang, K. Zhang, W. Chen, Y. Shen, J. Zhang, J. N. Zhang, and K. Kim, Global entangling gates on arbitrary ion qubits, *Nature* **572**, 363 (2019).
- [24] Y. Shapira, R. Shaniv, T. Manovitz, N. Akerman, L. Peleg, L. Gazit, R. Ozeri, and A. Stern, Theory of robust multiqubit nonadiabatic gates for trapped ions, *Phys. Rev. A* **101**, 032330 (2020).
- [25] N. Grzesiak, R. Blümel, K. Wright, K. M. Beck, N. C. Pienti, M. Li, V. Chaplin, J. M. Amini, S. Debnath, J.-S. Chen, and Y. Nam, Efficient arbitrary simultaneously entangling gates on a trapped-ion quantum computer, *Nat. Commun.* **11**, 1 (2020).
- [26] A. Soerensen and K. Moelmer, Quantum computation with ions in thermal motion, *Phys. Rev. Lett.* **82**, 1971 (1999).
- [27] A. Sørensen and K. Mølmer, Entanglement and quantum computation with ions in thermal motion, *Phys. Rev. A* **62**, 022311 (2000).
- [28] P. C. Haljan, K.-A. Brickman, L. Deslauriers, P. J. Lee, and C. Monroe, Spin-dependent forces on trapped ions

- for phase-stable quantum gates and entangled states of spin and motion, *Phys. Rev. Lett.* **94**, 153602 (2005).
- [29] P. J. Lee, K.-A. Brickman, L. Deslauriers, P. C. Haljan, L.-M. Duan, and C. Monroe, Phase control of trapped ion quantum gates, *J. Opt. B: Quan. Semi. Opt.* **7**, S371 (2005).
- [30] Y. Wu, S.-T. Wang, and L.-M. Duan, Noise analysis for high-fidelity quantum entangling gates in an anharmonic linear paul trap, *Phys. Rev. A* **97**, 062325 (2018).
- [31] S.-L. Zhu, C. Monroe, and L.-M. Duan, Trapped ion quantum computation with transverse phonon modes, *Phys. Rev. Lett.* **97**, 050505 (2006).
- [32] Y. Shapira, R. Shaniv, T. Manovitz, N. Akerman, and R. Ozeri, Robust entanglement gates for trapped-ion qubits, *Phys. Rev. Lett.* **121**, 180502 (2018).
- [33] A. E. Webb, S. C. Webster, S. Collingbourne, D. Braud, A. M. Lawrence, S. Weidt, F. Mintert, and W. K. Hensinger, Resilient entangling gates for trapped ions, *Phys. Rev. Lett.* **121**, 180501 (2018).
- [34] P. H. Leung, K. A. Landsman, C. Figgatt, N. M. Linke, C. Monroe, and K. R. Brown, Robust 2-qubit gates in a linear ion crystal using a frequency-modulated driving force, *Phys. Rev. Lett.* **120**, 020501 (2018).
- [35] A. R. Milne, C. L. Edmunds, C. Hempel, F. Roy, S. Mavadia, and M. J. Biercuk, Phase-modulated entangling gates robust to static and time-varying errors, *Phys. Rev. Applied* **13**, 024022 (2020).
- [36] P. Virtanen, R. Gommers, T. E. Oliphant, M. Haberland, T. Reddy, D. Cournapeau, E. Burovski, P. Peterson, W. Weckesser, J. Bright, S. J. van der Walt, M. Brett, J. Wilson, K. J. Millman, N. Mayorov, A. R. J. Nelson, E. Jones, R. Kern, E. Larson, C. J. Carey, Í. Polat, Y. Feng, E. W. Moore, J. VanderPlas, D. Laxalde, J. Perktold, R. Cimrman, I. Henriksen, E. A. Quintero, C. R. Harris, A. M. Archibald, A. H. Ribeiro, F. Pedregosa, P. van Mulbregt, and SciPy 1.0 Contributors, SciPy 1.0: Fundamental Algorithms for Scientific Computing in Python, *Nature Methods* **17**, 261 (2020).

Appendix A: Matrices expression

The expressions of the entries in matrices of Eq. (14) and Eq. (15) are given as the following.

$$\begin{cases} T_j^r = \int_0^{\tau_g} \sin(j\omega t) dt \\ T_j^i = \int_0^{\tau_g} \cos(j\omega t) dt \end{cases}, \quad (\text{A1})$$

$$\begin{cases} (\vec{a}_m^r)_j = -i\eta_m \int_0^{\tau_g} \sin(j\omega t) e^{i\nu_m t} dt \\ (\vec{a}_m^i)_j = -i\eta_m \int_0^{\tau_g} \cos(j\omega t) e^{i\nu_m t} dt \end{cases}, \quad (\text{A2})$$

$$\begin{cases} \theta_{jk}^{rr} = -2\eta_m^2 \int_0^{\tau_g} \int_0^{t_1} \sin(j\omega t_1) \sin(k\omega t_2) \\ \quad \times \sin(\nu_m(t_1 - t_2)) dt_1 dt_2 \\ \theta_{jk}^{ri} = -2\eta_m^2 \int_0^{\tau_g} \int_0^{t_1} \sin(j\omega t_1) \cos(k\omega t_2) \\ \quad \times \sin(\nu_m(t_1 - t_2)) dt_1 dt_2 \\ \theta_{jk}^{ir} = -2\eta_m^2 \int_0^{\tau_g} \int_0^{t_1} \cos(j\omega t_1) \sin(k\omega t_2) \\ \quad \times \sin(\nu_m(t_1 - t_2)) dt_1 dt_2 \\ \theta_{jk}^{ii} = -2\eta_m^2 \int_0^{\tau_g} \int_0^{t_1} \cos(j\omega t_1) \cos(k\omega t_2) \\ \quad \times \sin(\nu_m(t_1 - t_2)) dt_1 dt_2 \end{cases}, \quad (\text{A3})$$

where $j, k = n_s, n_s + 1, \dots, n_e$.

Appendix B: Initial phase robustness condition

Expressing the dependency of the Hamiltonian in Eq IID to the initial phase ϕ explicitly, we have

$$\begin{aligned}
\hat{\mathcal{H}}_{\text{car}} &= \sum_{j=1}^N \hbar \sigma_x^j \sum_{n=-\infty}^{\infty} [\Omega_n^r \cos(n\omega t + \phi) + \Omega_n^i \sin(n\omega t + \phi)] \\
&= \sum_{j=1}^N \hbar \sigma_x^j \sum_{n=0}^{\infty} [(\Omega_n^{rm} \sin(n\omega t) + \Omega_n^{im} \cos(n\omega t)) \sin \phi + (\Omega_n^{ic} \sin(n\omega t) + \Omega_n^{rc} \cos(n\omega t)) \cos \phi], \\
\hat{\mathcal{H}}_{\text{mot}} &= \sum_{m=0}^{N-1} \sum_{j=1}^N \hbar \eta_{j,m} (\hat{a}_m^\dagger e^{i\nu_m t} + \hat{a}_m e^{-i\nu_m t}) \sigma_x^j \sum_{n=-\infty}^{\infty} [-\Omega_n^r \sin(n\omega t + \phi) + \Omega_n^i \cos(n\omega t + \phi)] \\
&= \sum_{m=0}^{N-1} \sum_{j=1}^N \hbar \eta_{j,m} (\hat{a}_m^\dagger e^{i\nu_m t} + \hat{a}_m e^{-i\nu_m t}) \sigma_x^j \\
&\quad \sum_{n=0}^{\infty} [-(\Omega_n^{ic} \sin(n\omega t) + \Omega_n^{rc} \cos(n\omega t)) \sin \phi + (\Omega_n^{rm} \sin(n\omega t) + \Omega_n^{im} \cos(n\omega t)) \cos \phi].
\end{aligned} \tag{B1}$$

Having this Hamiltonian, we can also write the parameters in the evolution operator, the carrier phase Φ , the displacement in phase space α , and the accumulated geometric phase Θ as functions of the initial phase ϕ .

$$\begin{aligned}
\Phi(\phi) &= \vec{T}^T \vec{\Omega}^m \sin \phi + \vec{T}^T \vec{\Omega}^c \cos \phi \\
\alpha_m(\phi) &= \vec{a}_m^T \vec{\Omega}^c \sin \phi + \vec{a}_m^T \vec{\Omega}^m \cos \phi \\
\Theta_m(\phi) &= \vec{\Omega}^{cT} \tilde{\theta}_m \vec{\Omega}^c \sin^2 \phi + \vec{\Omega}^{mT} \tilde{\theta}_m \vec{\Omega}^m \cos^2 \phi - 2\vec{\Omega}^{cT} \tilde{\theta}_m \vec{\Omega}^m \sin \phi \cos \phi
\end{aligned} \tag{B2}$$

Therefore, the following conditions are necessary and sufficient for an initial phase robust gate.

$$\vec{T}^T \vec{\Omega}^c = \vec{T}^T \vec{\Omega}^m = 0, \tag{B3}$$

$$\vec{a}_m^T \vec{\Omega}^c = \vec{a}_m^T \vec{\Omega}^m = 0, \tag{B4}$$

$$\vec{\Omega}^{cT} \tilde{\theta}_m \vec{\Omega}^c = \vec{\Omega}^{mT} \tilde{\theta}_m \vec{\Omega}^m = \Theta_m, \tag{B5}$$

$$\vec{\Omega}^{cT} \tilde{\theta}_m \vec{\Omega}^m = 0 \tag{B6}$$

Appendix C: Sampling method for Fourier scheme

If we simply sample the Rabi-frequencies and phases at the discrete time intervals, the Fourier scheme introduces large errors as shown in Fig. 9. Here, we develop a sampling method to find the discrete functions which have the same Fourier expansion coefficients as the continuous one up to our truncation frequency. In IIB, we define the laser waveform of the blue-sideband transition $f(t)$ and expand it into Fourier series as the following.

$$f(t) = \Omega(t) e^{-i(\mu t + \phi(t))} = \sum_n \Omega_n \exp(-in\omega t) \tag{C1}$$

Here, we discretize $f(t)$ to be $f_{\text{seg}}(t)$ as the following.

$$f_{\text{seg}}(t) = e^{-i\mu t} h_{\text{seg}}(t) \tag{C2}$$

where

$$h_{\text{seg}}(t) = \sum_k \sum_n \Omega'_n e^{i(\mu - n\omega)k\tau_{\text{seg}}} g(t - k\tau_{\text{seg}}), \quad k = \frac{1}{2}, 1 + \frac{1}{2}, \dots, N_{\text{seg}} - \frac{1}{2}, \tag{C3}$$

where

$$\begin{aligned}\Omega'_n &= \frac{\Omega_n}{\text{sinc}\left(\frac{(\mu-n\omega)\tau_{\text{seg}}}{2}\right)}, \\ g(t) &= \begin{cases} 1, & |t| \leq \frac{1}{2}\tau_{\text{seg}}, \\ 0, & \text{otherwise} \end{cases}, \\ \text{sinc}(x) &= \frac{\sin x}{x}.\end{aligned}\tag{C4}$$

Here, to set the lower frequency components in the Fourier expansion of $f_{\text{seg}}(t)$ to be same as which in the continuous one, we need to modify Ω_n by a sinc function, as shown above. The norm and argument of $h_{\text{seg}}(t)$ is the segmented Rabi frequency and phase function.

Now, we will prove that the lower frequency components in the Fourier expansion are indeed equivalent when sampling using the formula given above. We first calculate the Fourier expansion of $f_{\text{seg}}(t)$. The coefficient of the m^{th} order in the Fourier series of $f_{\text{seg}}(t)$ is written as

$$\begin{aligned}F_{\text{seg}}(m) &= \frac{1}{\tau_g} \int_0^{\tau_g} f_{\text{seg}}(t) e^{im\omega t} dt \\ &= \frac{1}{\tau_g} \sum_n \sum_k \Omega'_n e^{i(\mu-n\omega)k\tau_{\text{seg}}} e^{i(m\omega-\mu)k\tau_{\text{seg}}} \frac{\sin\left(\frac{(\mu-m\omega)\tau_{\text{seg}}}{2}\right)}{\frac{\mu-m\omega}{2}} \\ &= \frac{\tau_{\text{seg}}}{\tau_g} \sum_n \sum_k \Omega'_n e^{i(m-n)\omega k\tau_{\text{seg}}} \text{sinc}\left(\frac{(\mu-m\omega)\tau_{\text{seg}}}{2}\right)\end{aligned}\tag{C5}$$

In the above equation, the summation of n can be divided into three cases. If $n = m$,

$$\frac{\tau_{\text{seg}}}{\tau_g} \sum_k \Omega'_m e^{i(m-m)\omega k\tau_{\text{seg}}} \text{sinc}\left(\frac{(\mu-m\omega)\tau_{\text{seg}}}{2}\right) = \frac{\tau_{\text{seg}}}{\tau_g} \Omega_m N_{\text{seg}} = \Omega_m\tag{C6}$$

If $n - m = qN_{\text{seg}}$, where q is a nonzero integer number,

$$\frac{\tau_{\text{seg}}}{\tau_g} \sum_k \Omega'_n e^{i(m-n)\omega k\tau_{\text{seg}}} \text{sinc}\left(\frac{(\mu-m\omega)\tau_{\text{seg}}}{2}\right) = \Omega'_{m+qN_{\text{seg}}} \text{sinc}\left(\frac{(\mu-m\omega)\tau_{\text{seg}}}{2}\right)\tag{C7}$$

otherwise,

$$\frac{\tau_{\text{seg}}}{\tau_g} \sum_k \Omega'_n e^{i(m-n)\omega k\tau_{\text{seg}}} \text{sinc}\left(\frac{(\mu-m\omega)\tau_{\text{seg}}}{2}\right) = 0\tag{C8}$$

Therefore, we have

$$F_{\text{seg}}(m) = \Omega_m + \sum_q \Omega'_{m+qN_{\text{seg}}} \text{sinc}\left(\frac{(\mu-m\omega)\tau_{\text{seg}}}{2}\right)\tag{C9}$$

Assume that, in the Fourier method, we truncate the frequency components from $-M$ to M , i.e. $\Omega_m = 0$ for $m > M$ and $m < -M$. Then, we require $N_{\text{seg}} > 2M$. In this case, we have

$$F_{\text{seg}}(m) = \begin{cases} \Omega_m, & -M \leq m \leq M \\ (-1)^q \frac{\mu - m'\omega}{\mu - m\omega} \Omega_{m'}, & qN_{\text{seg}} - M \leq m \leq qN_{\text{seg}} + M, \\ 0, & \text{Otherwise} \end{cases}\tag{C10}$$

with $m' = m - qN_{\text{seg}}$.

Hence, the remaining error of this sampling process comes from the terms where $qN_{\text{seg}} - M \leq m \leq qN_{\text{seg}} + M$, which would be a small number compared to $\Omega_{m-qN_{\text{seg}}}$ if $N_{\text{seg}} \gg 1$. Additionally, these are just high-frequency terms which would hardly contribute to the error. In addition, if we use segmented exponential functions as our basis to expand everything under these basis, the error can be further suppressed at the cost of slightly more complicated form for Eq.(14) and Eq.(15). In this case, the error terms in Eq.(C10) are automatically considered.

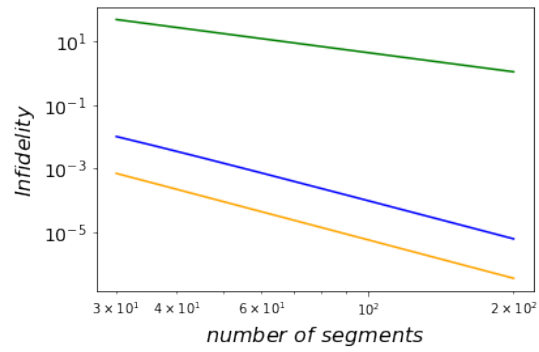


FIG. 9: The relations between the infidelity and the number of segments depending on the sampling methods. It is calculated from the example of Fig. 8. The sampling method of the orange line is the method introduced above. The sampling method of the blue(green) line is using the value of the middle(left-most) point for each segment. The infidelity is estimated by the Eq. 9. Infidelity of larger than 1 indicates larger values that the Eq. 9 can estimate.